Carbon 152 (2019) 715–726

Contents lists available at ScienceDirect

Carbon

journal homepage: www.elsevier.com/locate/carbon

Thermodynamic stability of nitrogen functionalities and defects in graphene and graphene nanoribbons from first principles

Michael Ayiania [a, 1], Alyssa J.R. Hensley [b, 1], Kyle Groden [b], Manuel Garcia-Perez [a, f], Jean-Sabin McEwen [a, b, c, d, e, *]

[a] Department of Biological Systems Engineering, Washington State University, Pullman, WA, 99164, USA
[b] Gene and Linda Voiland School of Chemical Engineering and Bioengineering, Pullman, WA, 99164, USA
[c] Department of Physics and Astronomy, Washington State University, Pullman, WA, 99164, USA
[d] Department of Chemistry, Washington State University, Pullman, WA, 99164, USA
[e] Institute for Integrated Catalysis, Pacific Northwest National Laboratory, Richland, WA, 99352, USA
[f] Bioproducts Sciences and Engineering Laboratory, Richland, WA, 99354, USA

ARTICLE INFO

Article history:
Received 11 January 2019
Received in revised form
20 May 2019
Accepted 4 June 2019
Available online 5 June 2019

ABSTRACT

Nitrogen functionalization of graphene significantly enhances the physical and chemical properties of graphitic materials, increasing their applicability as sorbents, heterogeneous catalysts, and electronic components. Being able to selectively induce different nitrogen functionalities via treatment conditions is key to the design and optimization of such materials. Here, we use density functional theory to study the thermodynamic stability of nitrogen functionalities in three graphene structures as a function of temperature and pressure, providing atomistic insight into the most favorable functionalized configurations. Phase diagrams show that nitrogen incorporation is most exergonic at graphene edges, with pyridinic groups dominating under the majority of conditions studied. For all nitrogen functionalities, lower temperatures and higher pressures result in the greater incorporation of nitrogen into the graphene structures. A density of states analysis shows that the stable pyridinic nitrogen structures induce new electronic states just below the Fermi level whose energy is tunable via nitrogen concentration and hence treatment temperature and pressure. Overall, we have characterized the thermodynamic stability of nitrogen functionalities within graphene and graphene nanoribbons, allowing for the directed tuning of such nitrogen groups experimentally and enabling the construction of more realistic models of nitrogenated graphene structures.

1. Introduction

Carbonaceous materials, such as graphene, activated carbon, and amorphous carbons, have garnered great interest in recent years as their physical, chemical, and electronic properties can be finely tuned through functionalization [1–3]. Such tuning is accomplished by changing the nature of the organic precursors and the method of activation, which in turn alters the surface chemistry through incorporation of heteroatoms (e.g. oxygen, hydrogen, sulfur, phosphorus, boron, and nitrogen) [4–8]. Property modification by controlling the surface chemistry of carbon-based materials has been shown to have tremendous technological implications for n-type graphene-based field effect transistors [9–12], electrochemical biosensors [13–16], lithium-ion batteries anodes [17,18], heterogeneous catalysts [19–30], wastewater treatment [31–38], and trace gas adsorption [39–43].

The value of nitrogen functionalization of graphene has been clearly demonstrated in three areas of application. First, nitrogen functionalized graphene has proven to be a great metal free electrochemical catalyst extensively used because of its low price, suitable activity for a variety of redox reactions, broad potential window, and relatively inert electrochemistry [44–49]. Second, in the area of hydrogen storage, an ideal non-polluting energy carrier with high energy density, the incorporation of nitrogen defects in graphene alone were shown to increase H_2 storage by 66% [50]. H_2 storage was further increased to 124% by combining nitrogen functionalization and Pd nanoparticles, where the strong binding of

* Corresponding author. Department of Biological Systems Engineering, Washington State University, Pullman, WA, 99164, USA.
E-mail address: js.mcewen@wsu.edu (J.-S. McEwen).
[1] These authors contributed equally.

https://doi.org/10.1016/j.carbon.2019.06.019
0008-6223/

Pd to nitrogen sites maintains the highly dispersed Pd [50,51]. Finally, the superior performance of nitrogen functionalized graphene at CO_2 storage relative to unmodified graphene was attributed to the strong interaction between nitrogen and CO_2 [52,53], with density functional theory (DFT) revealing strong electrostatic interactions between nitrogen sites and CO_2 due to their strong amphoteric properties [54].

There is a wealth of data on the various applications of nitrogen functionalized graphene. However, fundamental knowledge connecting the type of nitrogen structures—i.e. graphitic (direct substitution of a carbon atom within a graphite plane), pyridinic (edge nitrogen within a six-member ring), pyrrolic (edge nitrogen within a five-member ring)—formed during functionalization within a range of temperature and pressure conditions is often limited. Such knowledge gaps at the atomistic level make it difficult to construct experimentally realistic nitrogen-doped graphene computational models and molecularly design suitable materials. Some computational studies do not justify their choice of nitrogen-doped graphene models [55–58]. Other studies, e.g. nitrogen active sites in graphene for oxygen reduction reaction (ORR) in fuel cells, base their nitrogen-doped model surfaces on the simplest, most common nitrogen structures experimentally observed in an X-ray photoelectron spectroscopy (XPS) analysis of carbonaceous materials [59–68]. However, these model choices are complicated by the overlap between the carbon and nitrogen core level binding energies for different nitrogen functionalities, the many possible nitrogen configurations, and the difficulty of controlling the specific nitrogen doping configurations in carbon materials. A number of theoretical studies have explored the stability of different nitrogen configuration in graphene, but such studies do not consistently examine a wide range of nitrogen functionalities over different graphene models and their results are obtained at zero Kelvin and vacuum conditions [69–73]. Experimentally, nitrogen doping is performed under a wide range of temperature and pressure variations, which can significantly affect the types and concentration of nitrogen functionalities incorporated into carbonaceous materials.

Here, we provide atomistic insight into the most thermodynamically stable nitrogen functionalities in graphene using density functional theory (DFT). We computed Gibbs energies of reaction for the formation of different graphitic, pyridinic, and pyrrolic nitrogen functional groups as a function of temperature and NH_3 pressure on pristine graphene and graphene nanoribbons terminated with either hydrogen or a combination of hydrogen and oxygen. This includes nitrogen incorporation into carbon vacancies and non-hexagonal lattice structures. Activation of carbonaceous materials with ammonia has been described in recent years and was found to act as an activating agent, increasing the porosity of carbonaceous materials with increasing reaction time and temperature [74,75]. Phase diagrams of nitrogen functionalized graphene showed that nitrogen incorporation was exergonic at graphene edges and that pyridinic functionality was favorable under a wide range of experimental conditions, but thermodynamically competes with graphitic functionality under certain circumstances. Knowledge of the pressure and temperature dependence for different nitrogen functionalities in pristine graphene and graphene nanoribbons allows us to effectively tune the graphene electronic properties via treatment conditions. Overall, our work allows for the enhanced design of nitrogenated carbonaceous materials with applications in numerous fields.

2. Computational methods

DFT calculations were carried out using the Vienna *Ab Initio* Simulation Package (VASP) [76–78]. The projector-augmented wave (PAW) method [79,80] was used to model the core electrons (POTCARs released in 2002 for C, N, and O and 2001 for H) and a plane-wave basis set with an energy cutoff of 450 eV was used to model the valence electrons. To model the electron exchange and correlation, the Perdew-Burke-Ernzerhof (PBE) functional [81] was applied. Spin polarization was included in all calculations. The Gaussian smearing method was used to set partial occupancies of bands with a smearing width of 0.2 eV to facilitate Brillouin zone integration convergence, followed by extrapolation to zero Kelvin for total energy calculation [82,83]. All ground state optimizations used the conjugate gradient method and were considered converged when the relaxed interatomic cartesian forces were smaller than 0.025 eV/Å. The energy tolerance was set to 10^{-7} eV. Calculations for molecules in the gas phase were performed using an $18 \times 19 \times 20$ Å box using one single **k**-point, the Gamma point, to span the Brillouin zone.

Nitrogen functionalization was studied in three different graphene models (Fig. 1): a pristine graphene sheet ($14.8 \times 14.8 \times 20$ Å), a graphene nanoribbon with hydrogen terminated edges ($17 \times 29 \times 21$ Å), and a graphene nanoribbon with a mixture of hydrogen and oxygen terminated edges ($17 \times 29 \times 21$ Å). The graphene lattice constant was 2.467 Å, consistent with previous results [84–86]. The integration of the Brillouin zone was conducted using a $(3 \times 3 \times 1)$ Monkhorst-Pack grid [87] for pristine graphene, while a $(1 \times 2 \times 3)$ Monkhorst-Pack grid was used for the graphene nanoribbon models. All structures were visualized using VESTA [88].

Each of these models was functionalized with assorted nitrogen groups, discussed in detail in Section 3. The choice of defects here was informed by the work of Smith et al. who demonstrated the presence of defects such as vacancies, pentagonal and octagonal structures, and nitrogen defects in amorphous carbons derived from lingo-cellulosic materials [89,90]. The carbon defects studied here were the most populous defects and have been imaged with High Resolution Transmission Microcopy (HRTEM), a valuable tool to study and generate defects and monitor structural reconstructions in carbon nanostructures [91–93]. Banhart and Krasheninnikov have reviewed, theoretically and experimentally, how the electron beam of a transmission electron microscope (TEM) interacts with carbon nanostructures, changing their morphology via the generation, migration, and reconstructions of defects [94]. Types of defects include mono- and di-vacancies and stone-wales defects [95–101]. Evidence of such carbon defect structures have also been experimentally demonstrated by Iijima and coworkers [96]. Structures found to be common in the preceding study were examined here.

Due to the presence of oxygen functional groups in amorphous carbons derived from ligno-cellulosic materials [90,102], the concerted effect of oxygen and nitrogen defects was examined using a hydrogen + oxygen graphene nanoribbon model. Here, ether groups were introduced at the graphene edge due their relative stability compared to other oxygen functionalities like hydroxyl, carbonyl, and carboxyl [90,102].

The stability of all structures was determined via the calculation of Gibbs reaction energies according to:

$$\Delta G_{rxn} = E_{rxn} + \Delta\mu_{CH_4} - \Delta\mu_{NH_3} - \Delta\mu_{H_2} + G_{vib,defect} - G_{vib,intact} \quad (1)$$

In this equation, E_{rxn} is the zero-point corrected DFT reaction energy for the formation of the nitrogen doped structure within the specific graphene model used and is given explicitly in Section 3 (Equations (6)–(11)). $\Delta\mu_i$ is the chemical potential of the relevant gas phase species, calculated according to:

$$\Delta\mu_i(T,P) = \Delta\mu_i(T,P_0) - k_B T \ln\left(\frac{P}{P_0}\right) \quad (2)$$

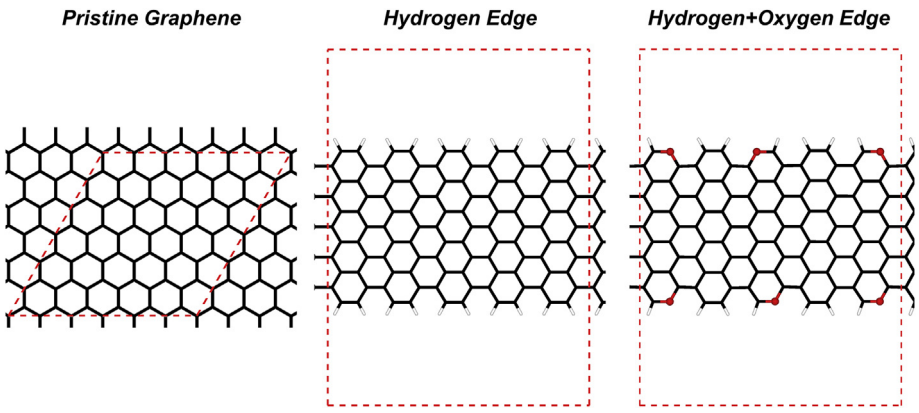

Fig. 1. Top views of the base models of pristine graphene, graphene nanoribbon terminated with hydrogen, and graphene nanoribbon terminated with hydrogen and oxygen with ether functionality. The black and white lines represent carbon and hydrogen, respectively, while the red spheres represent oxygen. The red dashed lines show the supercell boundaries. (A colour version of this figure can be viewed online.)

$$\Delta\mu_i(T,P_0) = [H(T,P_0) - H(0\ \mathrm{K},\ P_0)] - T[S(T,P_0) - S(0\ \mathrm{K},\ P_0)] \tag{3}$$

where T, P, P_0, k_B, H, and S are the temperature, pressure, reference pressure (1 bar), Boltzmann's constant, and gas phase enthalpies and entropies, respectively. The thermodynamic data required to calculate the chemical potentials as a function of pressure and temperature was taken from the JANAF thermochemical tables [103]. The gas phase composition was treated as 97 mol% NH_3, 1 mol% CH_4, 1 mol% H_2, and 1 mol% O_2.

The $G_{vib,intact}$ and $G_{vib,defect}$ terms in Equation (1) correspond to the vibrational contributions of the intact and defective graphene model free energies, computed using the harmonic oscillator approximation as:

$$G_{vib,i} = -k_B T \ln\left(\prod_{j=1}^{N_i} q_{vib,j}\right) \tag{4}$$

The vibrational partition function for the jth mode in this equation, $q_{vib,j}$, is defined as:

$$q_{vib,j} = \frac{1}{1 - \exp\left(-\frac{h\nu_j}{k_B T}\right)} \tag{5}$$

where ν_j is the vibrational frequency of the jth mode and N_i is the number of vibrational modes for the ith graphene model system. The zero-point energy ($ZPE = \sum_{j=1}^{N_i} \frac{h\nu_j}{2}$) has been subsumed into the reaction energy of Equation (1). The vibrational frequencies for the graphene model structures were computed by allowing all atoms to relax with the exception of two rows of atoms along the short axis in the nanoribbon models (Fig. S1) to avoid inclusion of vibrations propagating throughout the entire unit cell that require careful treatment using a more sophisticated analysis. Additionally, any computed modes captured poorly with the harmonic oscillator approximation (i.e. modes with imaginary magnitude), were modeled using a recently developed approximation that calculates partition functions for the normal coordinates associated with these errorneous modes through explicit evaluation of the potential energy surface along said coordinate [104,105].

3. Results and discussion

3.1. Pristine graphene

Different defects and nitrogen functional groups were created on a pristine graphene sheet and the reaction energies for the formation of these defects were calculated according to Equations (6) and (7):

$$C_x + nNH_3 + \frac{4m-3n}{2}H_2 \rightarrow C_{x-m}N_n + mCH_4 \tag{6}$$

$$E_{rxn} = \left(E_{C_{x-m}N_n} + mE_{CH_4}\right) - \left(E_{C_x} + nE_{NH_3} + \frac{4m-3n}{2}E_{H_2}\right) \tag{7}$$

where $E_{C_{x-m}N_n}$, $E_{C_xH_y}$, E_{CH_4}, E_{H_2}, and E_{NH_3} are the DFT-calculated total energies of the nitrogen doped graphene, pristine graphene, gas phase methane, gas phase hydrogen, and gas phase ammonia. x is the number of carbon atoms in the pristine graphene sheet; n is the number of nitrogen groups created; and m is the number of carbon defects created ($m \geq n$). As shown in Fig. 2, the types of defects tested here involve: (1) replacement of graphitic carbon with nitrogen in the absence of other defects, i.e. graphitic nitrogen (GN); (2) two graphitic nitrogen within the same six-membered ring in para (2 GN-Para), ortho (2 GN-Ortho), or meta (2 GN-Meta) positions; and (3) pyridinic (P_6N) or pyrrolic (P_5N) functional groups within existing graphitic defects, i.e. single, double, and triple carbon vacancies (SV, DV, and TV, respectively) as well as the 585 defect which contains two 5-membered rings and an 8-membered ring. The DFT-based reaction energies for all structures are summarized in Table S1. We note that during optimization of nitrogen-doped single vacancy (SV) structures, the vacancy is repaired by the formation of a 5-membered ring, as shown in structure P_6N-SV in Fig. 2. This result agrees with previous mechanistic studies of graphitic nitrogen doping in thermally treated graphene with ammonia [106].

The most favorable structures at zero Kelvin under vacuum conditions are the $4P_6N$-DV ($E_{rxn} = 0.43$ eV) and GN ($E_{rxn} = 0.64$ eV) structures. The next most favorable structures are the 2GN-Para ($E_{rxn} = 1.31$ eV), $3P_6N$-SV ($E_{rxn} = 1.60$ eV), and 2 GN-Meta ($E_{rxn} = 1.71$ eV). For the two graphitic nitrogen structures, 2GN-Para is more stable than both 2 GN-Ortho and 2 GN-Meta, which agrees with the calculated repulsive interactions between two nitrogen atoms within defect-free graphene as a function of interatomic distance [86].

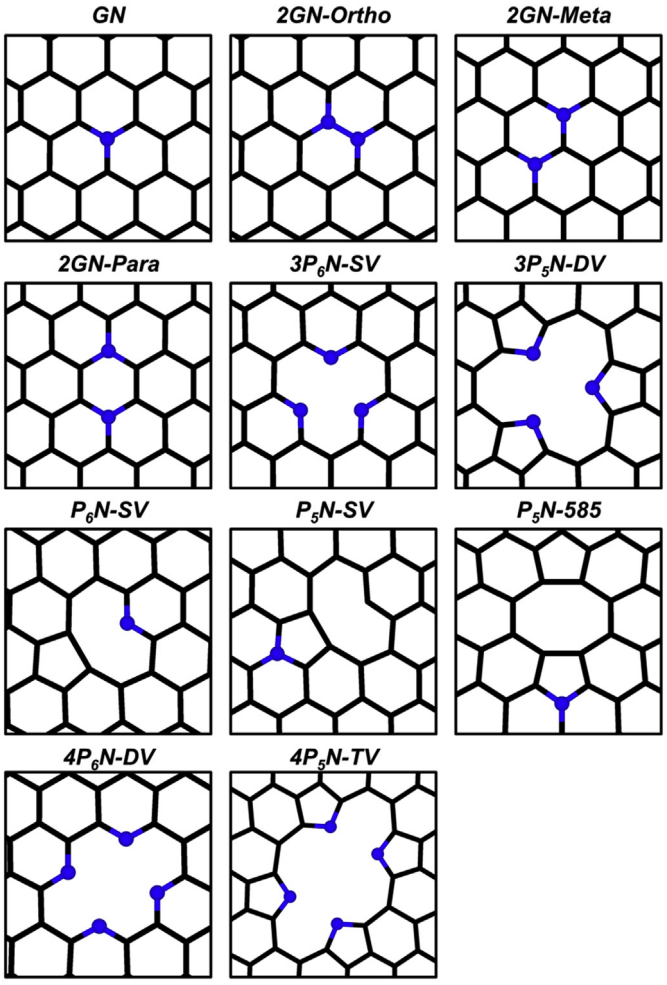

Fig. 2. Top views of nitrogenated groups on a pristine graphene sheet. Species are graphitic nitrogen (GN), two para graphitic nitrogen (2 GN-Para), two ortho graphitic nitrogen (2 GN-Ortho), two meta graphitic nitrogen (2 GN-Meta), pyridinic nitrogen at single and double vacancies (P_6N-SV, 3P_6N-SV, 4P_6N-DV), and pyrrolic nitrogen at single, double, and triple vacancies (P_5N-SV, 3P_5N-DV, 4P_5N-TV) as well as incorporated into the 585 defect structure (P_5N-585), which has a two 5-membered rings and an 8-membered ring. The black lines represent C while the blue spheres represent N. Only a portion of the unit cell is shown in order to highlight the defects and side views are shown in Fig. S2. (A colour version of this figure can be viewed online.)

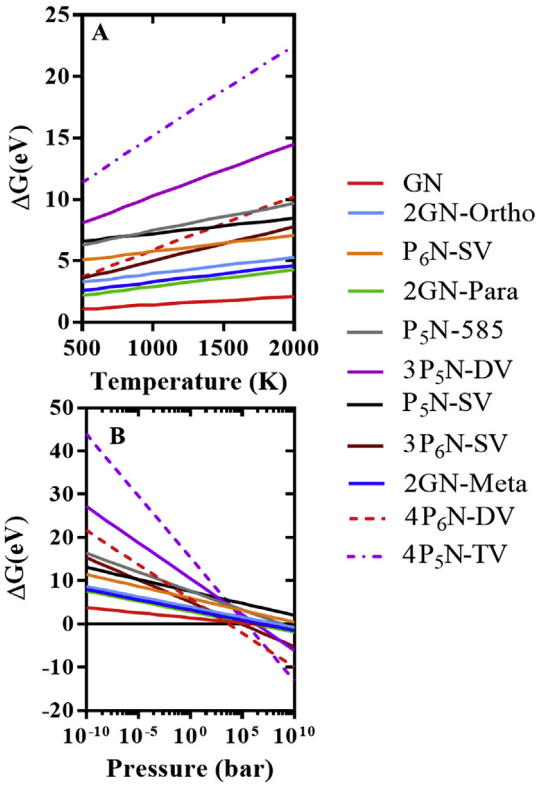

Fig. 3. Phase diagram of nitrogen defect structures on pristine graphene with respect to (A) temperature at 1 bar and (B) pressure at 800 K. Pristine graphene is the reference structure at $\Delta G = 0$ eV in both graphs. Top views of all the nitrogen defect graphene structures referenced here are shown in Fig. 2. (A colour version of this figure can be viewed online.)

In order to fully investigate the stability of nitrogen defects in pristine graphene under more realistic conditions, we calculated the Gibbs reaction energies for the formation of each structure as a function of temperature and pressure, as shown in Fig. 3. Note that lower Gibbs reaction energies are indicative of more favorable reactions. As the temperature is varied from 500 to 2000 K at 1 bar (Fig. 3A), GN is the most stable of the defect structures. However, pristine graphene is still the most favorable overall. Furthermore, increasing the temperature makes all of the defect structures less stable. As the pressure is varied from 10^{-10}–10^{10} bar at a fixed temperature of 800 K (Fig. 3B), all structures become more stable as the reaction equilibrium is shifted towards defect formation. At extremely high pressures (>10^5 bar), the 4P_5N-TV, 4P_6N-DV, 3P_5N-DV, and 3P_6N-SV defects become more stable than pristine graphene. This agrees well with other theoretical studies showing that the concentration of nitrogen around defects increases at larger NH_3 pressures [25]. Furthermore, the formation of the 4P_6N-DV structure is potentially quite significant to the performance of carbonaceous materials as such structures have been proposed to be responsible for the introduction of a large electron donor state in nitrogen-doped carbon nanotubes [107]. Overall, excluding pristine graphene, the most thermodynamically-stable nitrogen-doped structures are the GN, 4P_5N-TV, and 4P_6N-DV conformations.

The effect of the most thermodynamically favorable nitrogen functionalities on the electronic properties of pristine graphene was analyzed by calculating the density of states. From the total density of states (TDOS) shown in Fig. 4A, the creation of GN defects shifts the center of the valence band (calculated as $\varepsilon = \int_{-\infty}^{E_F} \rho(E)EdE$, where $\rho(E)$ was normalized and E_F is the Fermi energy level) away from the Fermi level (−9.09 eV to −9.72 eV, see Table S2) and induces additional states just above the Fermi level (peak centered at 0.1 eV). These new states are localized on the nitrogen atom's *p*-states, as shown in the nitrogen local density of states (LDOS) in Fig. 5A, and suggest that GN defects would enhance the electron conduction of pristine graphene. Different from the GN defect, the pyrrolic and pyridinic nitrogen defects (4P_5N-TV and 4P_6N-DV) either shift the center of the valence band toward the Fermi level to −8.72 eV or have a minimal effect ($\varepsilon = -9.12$ eV), respectively, as shown in Fig. 4A. This suggests that the formation of the 4P_5N-TV defect causes the graphene material as a whole to more readily bind adspecies. Furthermore, 4P_5N-TV and 4P_6N-DV create new states localized on the nitrogen atoms just below the Fermi level (Fig. 5A). The localization of the high energy (near Fermi level) induced states on the defect nitrogen suggests that these defects could strongly bind adspecies, acting as potential binding sites for transition metal atoms or nanoparticles for catalyst materials or for wastewater filtration [25,29,108].

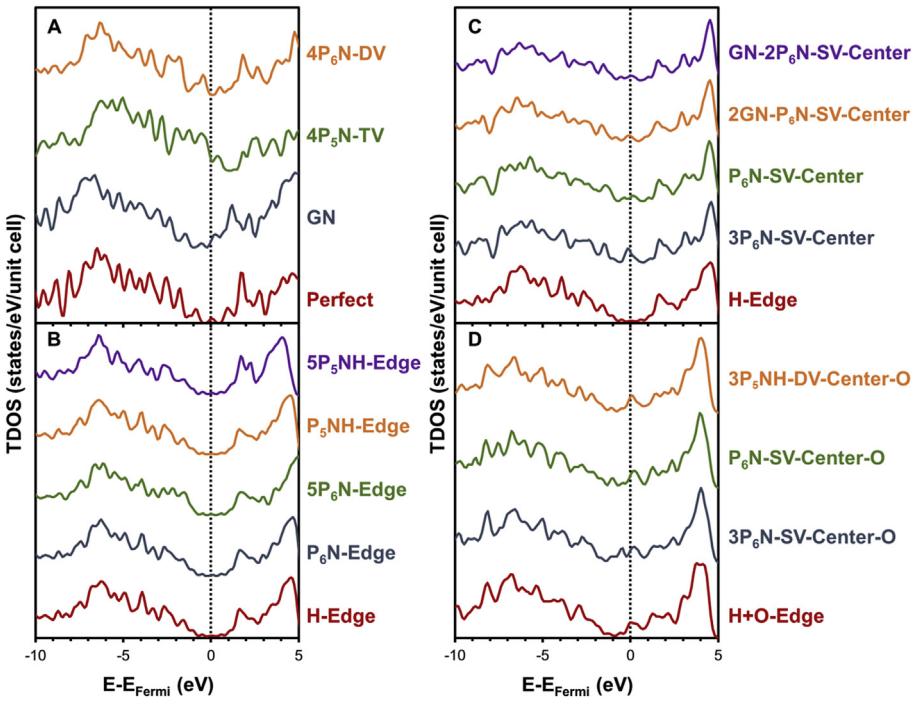

Fig. 4. TDOS of the most thermodynamically stable nitrogen-doped (A) pristine graphene (structures in Fig. 2), (B) hydrogen-edge graphene with edge only dopants (structures in Fig. 6), (C) hydrogen-edge graphene with center only dopants (structures in Fig. 9), and (D) hydrogen-oxygen edge graphene with center only dopants (structures in Fig. 11). (A colour version of this figure can be viewed online.)

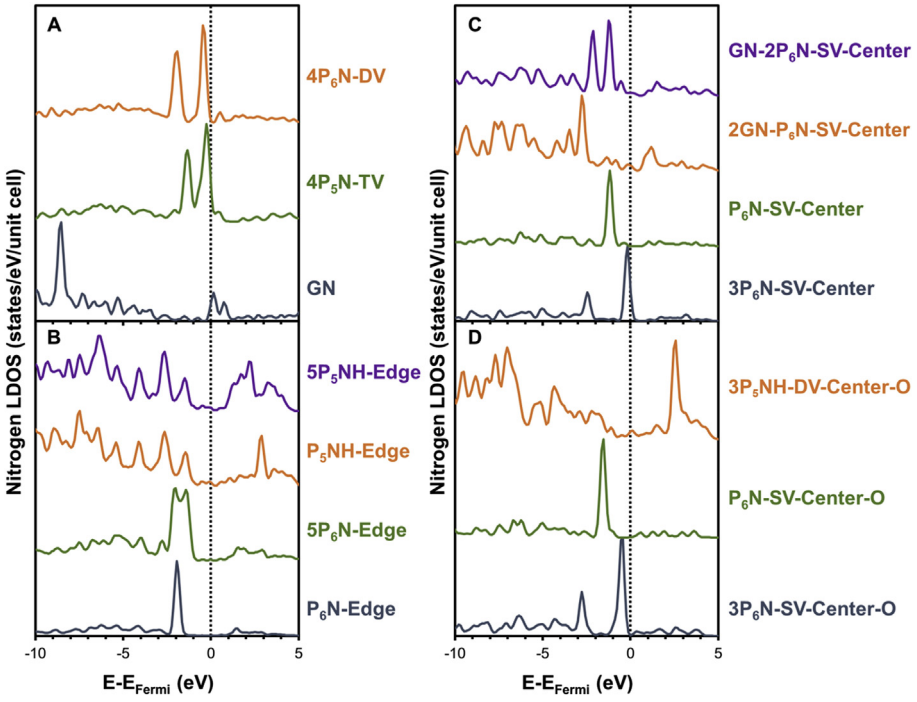

Fig. 5. Summed LDOS for all nitrogen atoms within the most thermodynamically stable nitrogen-doped (A) pristine graphene (structures in Fig. 2), (B) hydrogen-edge graphene with edge only dopants (structures in Fig. 6), (C) hydrogen-edge graphene with center only dopants (structures in Fig. 9), and (D) hydrogen-oxygen edge graphene with center only dopants (structures in Fig. 11). (A colour version of this figure can be viewed online.)

3.2. Hydrogen-edge graphene

The effect of edges on nitrogen incorporation is critical as Smith et al. has shown that the structure of amorphous carbon produced from lignocellulosic materials grows from $C_{22}H_{10}O_5$ at 673 K to $C_{37}H_{12}O_3$ at 973 K [102], meaning that chars are small and highly defective polyaromatic systems with high edge concentrations. Nitrogen was incorporated both at the edge and the center of the

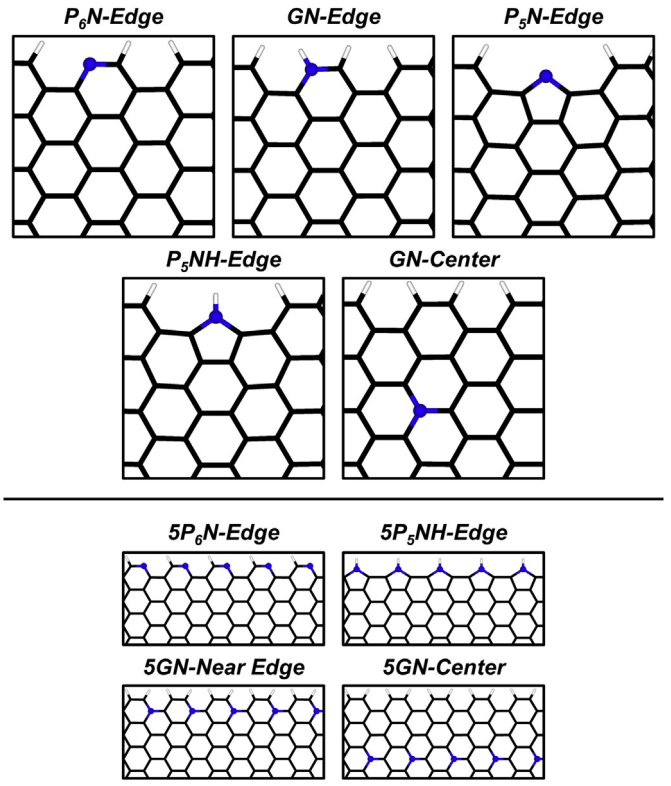

Fig. 6. Top views of nitrogenated defects on the hydrogen-edge graphene model. Top panel shows isolated nitrogen defects (1 nitrogen/20 edge carbon atoms). Species are monomerized pyridinic edge (P_6N-Edge), graphitic nitrogen at the edge (GN-Edge), monomerized pyrrolic without H (P_5N-Edge), monomerized pyrrolic with H (P_5NH-Edge), and graphitic nitrogen at the center (GN-Center). Bottom panel shows the high concentration (5 nitrogen atoms/20 edge carbon atoms) defects. Species are pyridines (5P_6N-Edge), pyrrolics with H (5P_5NH-Edg), graphitic nitrogens at the edge (5 GN-Edge), and graphitic nitrogens at the center (5 GN-Center). The black and white lines represent C and H, respectively, while the blue spheres represent N. Only a portion of the unit cell is shown in order to highlight the defects and side views are shown in Fig. S3. (A colour version of this figure can be viewed online.)

graphene nanoribbon sheet. Additionally, the effect of the nitrogen edge concentration was also studied here. The DFT reaction energies for the formation of these defects were calculated according to Equations (8) and (9):

$$C_xH_y + nNH_3 + \frac{(4m + y^*) - (3n + y)}{2}H_2 \rightarrow C_{x-m}N_nH_{y^*} + mCH_4 \quad (8)$$

$$E_{rxn} = \left(E_{C_{x-m}N_nH_{y^*}} + mE_{CH_4}\right) - \left(E_{C_xH_y} + nE_{NH_3} + \frac{(4m + y^*) - (3n + y)}{2}E_{H_2}\right) \quad (9)$$

where $E_{C_{x-m}N_nH_{y^*}}$, $E_{C_xH_y}$, E_{CH_4}, E_{H_2}, and E_{NH_3} are the DFT-calculated total energies of the nitrogen-doped hydrogen-edge graphene, hydrogen-edge graphene, gas phase methane, gas phase hydrogen, and gas phase ammonia; x is the number of carbon atoms in the hydrogen-edge sheet; y is the number of hydrogen atoms in the initial hydrogen-edge graphene model; y^* is the number of hydrogen atoms in nitrogen defect structure; n is the number of nitrogen defects created; and m is the of carbon defects created ($m \geq n$).

3.2.1. Edge nitrogen functionalities

For the isolated nitrogen dopants on the hydrogen-edge graphene model, all of the tested structures are shown in Fig. 6 and the DFT-based reaction energies are summarized in Table S3. The types of structures tested here are monomerized pyridinic nitrogen (P_6N-Edge), monomerized pyrrolic nitrogen (P_5NH-Edge), monomerized pyrrolic nitrogen without hydrogen (P_5N-Edge), graphitic nitrogen at the edge (GN-Edge), and a graphitic nitrogen in the ribbon center (GN-Center). According to the DFT reactions energies, P_5NH-Edge ($E_{rxn} = -0.46$ eV), GN-Edge ($E_{rxn} = 0.02$ eV), and P_6N-Edge ($E_{rxn} = 0.07$ eV) are the most favorable nitrogen defect structures (Table S3). Notably, the DFT energies show that the formation of nitrogen functional groups is much more favorable at the edge of the hydrogen model than in the pristine graphene sheet. This is consistent with experiments that show nitrogen incorporation at the edges of graphene nanoribbons and n-type materials upon ammonia exposure under high temperatures [9].

The effect of temperature and pressure on the thermodynamic stability of the different isolated nitrogen edge defects is shown in Fig. 7. Different from nitrogen defects in pristine graphene (Fig. 3), the formation of several of the nitrogen defects on a hydrogen terminated graphene edge are exergonic. As shown in Fig. 7A, the temperature effects at 1 bar show that P_6N-Edge is the most stable defect structure over the entire temperature range, followed by the non-defect hydrogen-edge graphene and P_5NH-Edge. Finally, a comparison between the GN-Edge and GN-Center results show that, over the entire temperature and pressure range studied, nitrogen substitution is more favorable on the edge of graphene than in the center by ~0.5 eV.

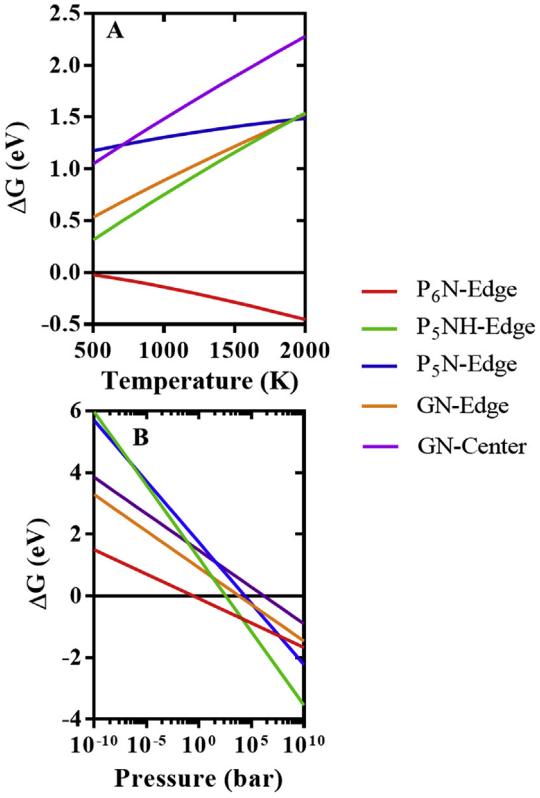

Fig. 7. Phase diagram of isolated nitrogen functional groups on the hydrogen-edge graphene model with respect to (A) temperature at 1 bar and (B) pressure at 800 K. The intact hydrogen-edge graphene sheet is the reference structure at $\Delta G = 0$ eV in both graphs. Species labels refer to structures shown in Fig. 6. (A colour version of this figure can be viewed online.)

To assess the effects of high nitrogen defect concentration within the edge, one side of the graphene sheet was saturated with three types of nitrogen defects (Fig. 6). As shown in Fig. 8A, the pyridinic ($5P_6N$-Edge) defect structure remains the most favorable over the entire temperature range at edge saturation. As the pressure is varied at a fixed temperature (Fig. 8B), the pyridinic structure with a high nitrogen concentration ($5P_6N$-Edge) is the most thermodynamically stable in the lower pressure regime while pyrrolic groups ($5P_5NH$-Edge) are stable at higher pressures values. One interesting point here is while the monomerized pyrrolic group tends to be more favorable at lower temperatures (Fig. 7A), the stability of these functional groups significantly decreases as the nitrogen content in the edges increases (Fig. 8A). However, pyridines, whether monomerized or at edge saturation concentrations, are more favorable than the rest of the tested structures. Therefore, under a wide range of temperatures, pressures, and dopant concentrations, the majority of nitrogen defects formed in carbonaceous materials are pyridine-like functional groups.

Similar to the pristine graphene systems, we calculated the electronic properties of the most thermodynamically favorable nitrogen defects for the isolated and saturated defect concentrations in the hydrogen-edge graphene model. As shown in Fig. 4B and Table S2, the incorporation of nitrogen into the hydrogen-edge graphene does not significantly shift either the valence or the conduction bands or induce new states near the Fermi level. The latter is due to the lack of nitrogen states near the Fermi level (−1 to 1 eV, Fig. 5B). Compared to the nitrogen LDOS of the pyrrolic and pyridinic structures within pristine graphene (Fig. 5A), the nitrogen incorporated along the hydrogen-edge are electronically less accessible for bonding adspecies, seen in the downshifted highest occupied nitrogen bands for the edge nitrogen (Fig. 5B). Overall, nitrogen functionalization of a hydrogen terminated graphene edge does not significantly alter its electronic structure, making such nitrogen defects unlikely to outperform graphene edges alone in the binding of metal centers or molecular pollutants.

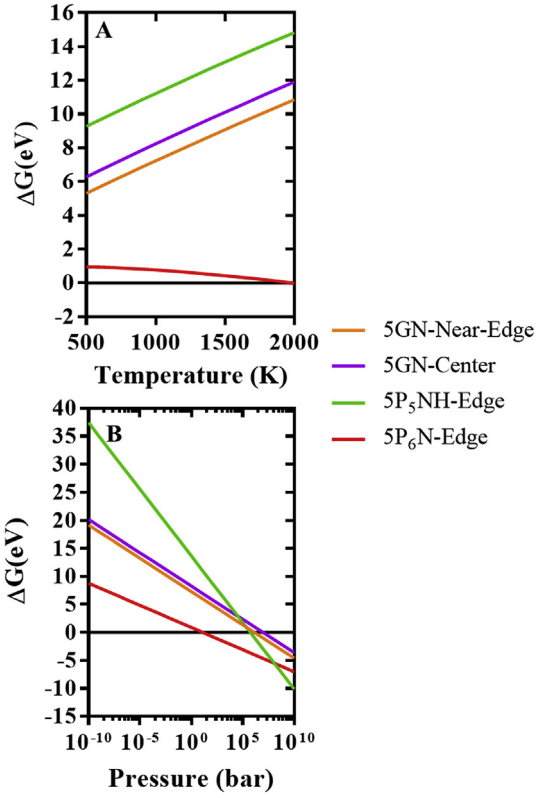

Fig. 8. Phase diagram of edge saturated nitrogen defect structures on hydrogen-edge graphene with respect to (A) temperature at 1 bar and (B) pressure at 800 K. The intact hydrogen-edge graphene sheet is the reference structure at $\Delta G = 0$ eV in both graphs. Species labels refer to structures shown in Fig. 6. (A colour version of this figure can be viewed online.)

3.2.2. Center nitrogen functionalities with defects

To better simulate complex carbonaceous materials like chars, nitrogen functionalization of carbon vacancies within our hydrogen-edge graphene nanoribbon model was examined using the structures shown in Fig. 9: (1) single carbon vacancies with pyridinic (P_6N-SV-Center, $3P_6N$-SV-Center), pyrrolic (P_5N-SV-Center), graphitic (GN-SV-Center, 3GN-SV-Center), and mixed functionality (2 GN-P_6N-SV-Center and GN-$2P_6N$-SV-Center) nitrogen; (2) double carbon vacancies with pyridinic ($4P_6N$-DV-Center) and pyrrolic (P_5NH-DV-Center, $3P_5N$-DV-Center, $3P_5NH$-DV-Center) nitrogen; and (3) triple carbon vacancies with pyrrolic ($4P_5N$-TV-Center) nitrogen. As noted previously for the pristine graphene structures, carbon vacancies created in the initial structure can reconstruct in the presence of nitrogen, forming non-hexagonal rings after optimization.

DFT energies calculated for these structures at zero Kelvin under vacuum conditions (Table S4) show 2 GN-P_6N-SV-Center ($E_{rxn} = -1.07$ eV), GN-$2P_6N$-SV-Center ($E_{rxn} = -0.82$ eV), $3P_5NH$-DV-Center ($E_{rxn} = -0.27$ eV), and 3 GN-SV-Center ($E_{rxn} = -0.04$ eV) to be the most favorable structures followed by $4P_6N$-DV-Center ($E_{rxn} = 0.36$ eV), P_5NH-DV-Center ($E_{rxn} = 0.68$ eV), and $4P_5N$-TV-Center ($E_{rxn} = 0.71$ eV). Fig. 10 shows the phase diagrams constructed using these center nitrogen-functionalized defect structures in hydrogen-edge graphene. At 1 bar, the pyridinic defects are the most stable across the studied temperature range (Fig. 10A), with the most favorable structure being GN-$2P_6N$-SV-Center from 500 to 1600 K, 2GN-P_6N-SV-Center from 500 to 1100 K, and P_6N-SV-Center for temperatures greater than 1600 K. The next most favorable structures at 1 bar are $3P_6N$-SV-Center, 3GN-SV-Center, and GN-SV-Center. Similar to the nitrogen defect creation in pristine graphene (Fig. 3), the formation of these defect structures in hydrogen-edge graphene is endergonic at 800 K until the pressure reaches 10^4 bar (Fig. 10B), suggesting that these defects are much less likely to form as compared to nitrogen incorporation into the edge (Figs. 7 and 8). Within a particular defect type (i.e. pyridinic and graphitic), increasing the pressure or decreasing the temperature favors higher nitrogen concentration defect structures, suggesting that the nitrogen incorporation thermodynamically stabilizes the carbon vacancies. These results suggest that the distribution and concentration of nitrogen groups can be controlled by the temperature and pressure, which will inform the experimental functionalization of carbonaceous materials with nitrogen.

As shown in Fig. 4C, the TDOS for the most stable structures of nitrogen functionalized carbon vacancies in hydrogen-edge graphene shows a similar trend to that observed for pristine graphene (Fig. 4A). Namely, the creation of only pyridinic functional groups (P_6N-SV-Center and $3P_6N$-SV-Center) induces new states to appear in the TDOS just below the Fermi level (Fig. 4C), which are localized on the nitrogen atoms (Fig. 5C). Interestingly, a comparison of the nitrogen LDOS for the P_6N-SV-Center (Fig. 5C), $3P_6N$-SV-Center (Fig. 5C), and 4P6N-DV (Fig. 5A) structures show that the highest occupied nitrogen band approaches the Fermi level as the number of pyridinic nitrogen increases. This suggests that the bond strength of adspecies on nitrogen-doped carbonaceous materials can be tuned via the incorporation of more or less pyridinic nitrogen species, which we have shown above to be controllable through the temperature and pressure used during the nitrogen doping process. However, this pyridinic nitrogen tuning effect on the highest

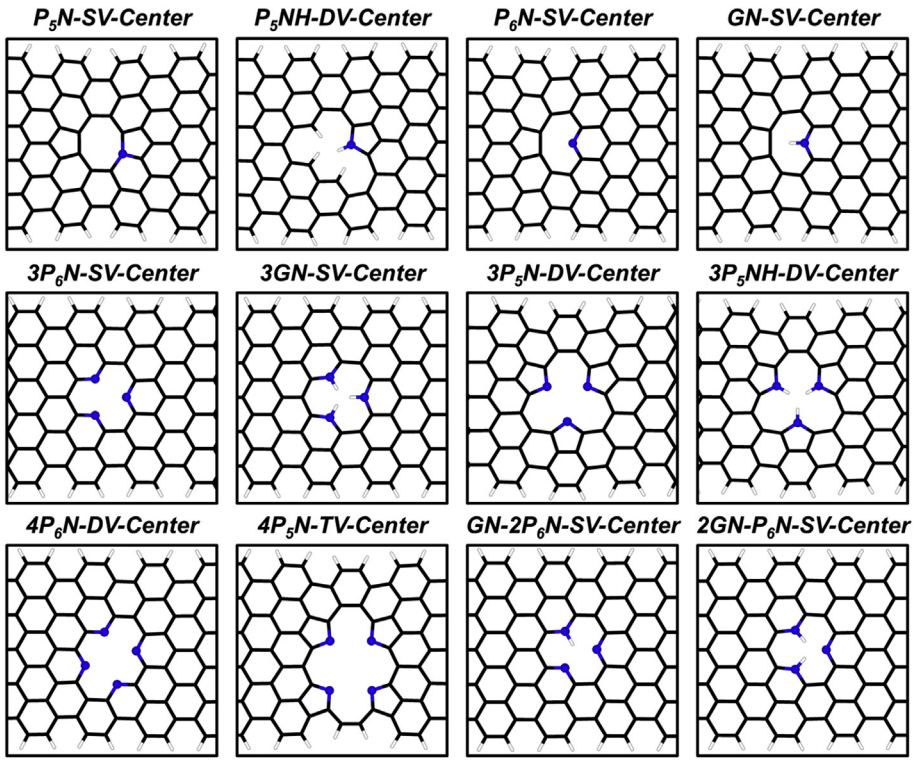

Fig. 9. Top views of nitrogenated defects on carbon vacancies and non-hexagonal defects on hydrogen-edge graphene. Species are: P_5N-SV-Center, P_6N-SV-Center, $3P_6$N-SV-Center, 3GN-SV-Center, GN-SV-Center, $2GN\text{-}P_6$N-SV-Center, and $GN\text{-}2P_6$N-SV-Center on single carbon vacancy defects; $3P_5$N-DV-Center, $3P_5$NH-DV-Center, $4P_6$N-DV-Center, and P_5NH-DV-Center on double carbon vacancy defects; and $4P_5$N-TV-Center on triple carbon vacancy defects. The black and white lines represent carbon and hydrogen, respectively, while the blue spheres represent nitrogen. Only a portion of the unit cell is shown in order to highlight the defects and side views are shown in Fig. S4. (A colour version of this figure can be viewed online.)

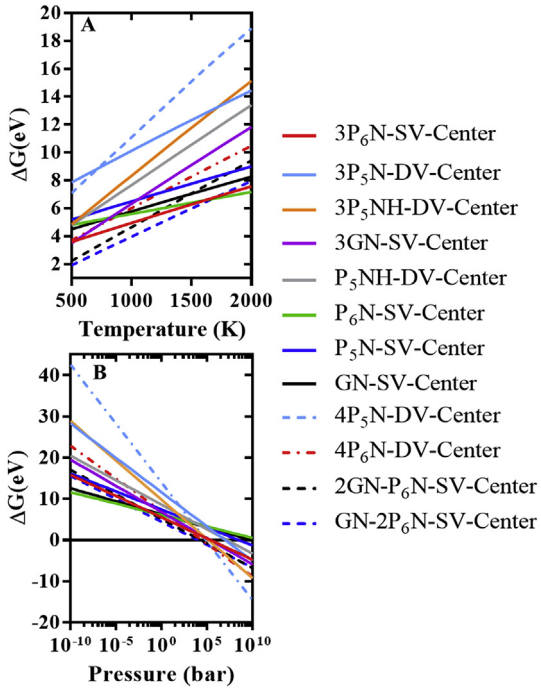

Fig. 10. Phase diagram of nitrogen defect structures on carbon vacancies and non-hexagonal defects on hydrogen-edge graphene with respect to (A) temperature at 1 bar and (B) pressure at 800 K. The intact hydrogen-edge graphene sheet is the reference structure at $\Delta G = 0$ eV in both graphs. Species labels refer to structures shown in Fig. 9. (A colour version of this figure can be viewed online.)

occupied nitrogen band can be affected by the simultaneous formation of GN functionality at the vacancy (see structures $GN\text{-}2P_6$N-SV-Center and 2 $GN\text{-}P_6$N-SV-Center in Fig. 5C). Similar to the pristine graphene models, the formation of GN functionality induces nitrogen states above the Fermi level, thus the GN may possess n-type conductivity since nitrogen has one additional electron compared to a carbon atom and thus making such systems more likely to bind cationic pollutants [73]. Overall, these results show: (1) there is minimal electronic interaction between the nitrogen functionalized carbon vacancies and a hydrogen-edge graphene edge and (2) that the electronic properties of the nitrogen-doped graphene can be tuned via the concentration of pyridinic nitrogen.

3.3. Hydrogen and oxygen edge graphene

Often in carbonaceous materials like the amorphous carbons produced from lignocellulosic materials at low carbonization conditions, it is difficult to avoid the formation of oxygen functional groups. Previous experimental and theoretical work has determined the dominant oxygen functionality in amorphous carbonaceous materials at temperatures over 973 K to be ether groups [102]. Other oxygenated functional groups (i.e. hydroxyl, carbonyl, and carboxyl) can be found in amorphous carbons oxidized at low temperature (below 573 K) but are unstable at temperatures over 773 K [109,110]. In order to examine the potential interaction between such oxygen functional groups and nitrogen functionalization, the graphene nanoribbon model was modified to incorporate ether groups along the edge. The DFT reaction energies for the formation of these defects were calculated according to Equations (10) and (11):

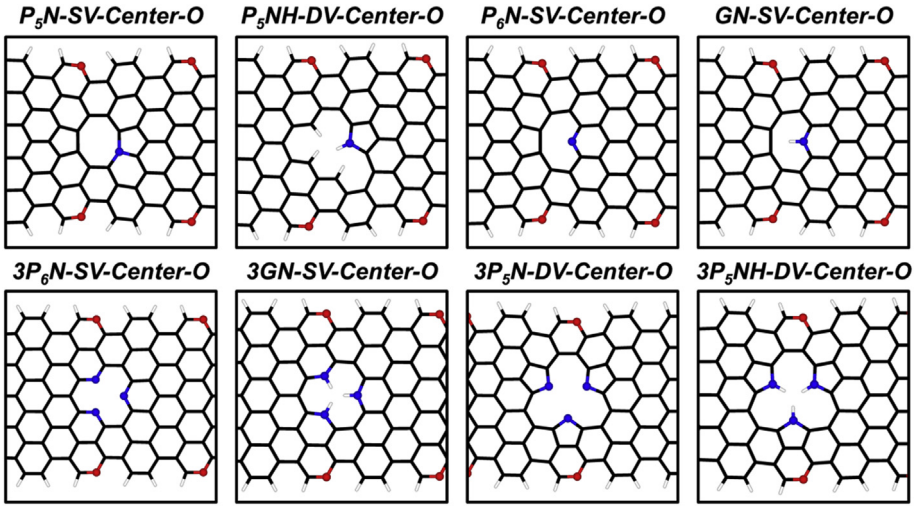

Fig. 11. Top views of nitrogenated defects on vacancies and non-hexagonal defects on hydrogen-oxygen edge graphene. Species are: P_5N-SV-Center-O, P_6N-SV-Center-O, $3P_6$N-SV-Center-O, 3GN-SV-Center-O, and GN-SV-Center-O on single carbon vacancy defects; $3P_5$N-DV-Center-O, $3P_5$NH-DV-Center-O, $4P_6$N-DV-Center-O, and P_5NH-DV-Center-O on double vacancy defects; and $4P_5$N-TV-Center-O on a triple carbon vacancy defect. The black and white lines represent C and H, respectively, while the blue and red spheres represent N and O, respectively. Only a portion of the unit cell is shown in order to highlight the defects and side views are shown in Fig. S5. (A colour version of this figure can be viewed online.)

$$C_xH_yO_Z + nNH_3 + \frac{(4m + y^*) - (3n + y)}{2}H_2 \rightarrow C_{x-m}N_nH_{y^*}O_z + mCH_4 \quad (10)$$

$$E_{rxn} = \left(E_{C_{x-m}N_nH_{y^*}O_Z} + mE_{CH_4}\right) - \left(E_{C_xH_yO_z} + nE_{NH_3} + \frac{(4m + y^*) - (3n + y)}{2}E_{H_2}\right) \quad (11)$$

where $E_{C_{x-m}N_nH_{y^*}O_z}$, $E_{C_xH_yO_z}$, E_{CH_4}, E_{H_2}, and E_{NH_3} are the DFT-calculated total energies of the nitrogen defected hydrogen-oxygen edge graphene, hydrogen-oxygen edge graphene, gas phase methane, gas phase hydrogen, and gas phase ammonia; x is the number of carbon atoms in the hydrogen-edge sheet; y is the number of hydrogen atoms in the initial hydrogen-oxygen edge graphene model; y^* is the number of hydrogen atoms in nitrogen defect structure; z is the number of oxygen atoms; n is the number of nitrogen defects created; and m is the of carbon defects created ($m \geq n$).

Fig. 11 shows the nitrogen defect structures examined in the hydrogen-oxygen edge graphene. The DFT reactions energies show that the $3P_5$NH-DV-Center-O ($E_{rxn} = 0.15$ eV), 3GN-SV-Center-O ($E_{rxn} = 0.49$ eV) and P_5N-SV-Center-O ($E_{rxn} = 0.50$ eV)—i.e. the trimerized pyrrolic, trimerized graphitic, and monomerized pyrrolic nitrogen in the center of the graphene sheet, respectively—are the most stable structures at zero Kelvin under vacuum conditions. All DFT reactions energies are shown in Table S5.

Introducing the effect of temperature shows pyridine structures to be the most favorable nitrogen-doped structures over the entire temperature range at 1 bar (Fig. 12A), consistent with the previous models and showing that the pyridinic functionality is overall the most thermodynamically favorable structure under a number of different surface conditions. Increasing the pressure at 800 K to above 10^5 bar causes a transition to pyrrolic groups ($3P_5$NH-DV-Center-O, Fig. 12B). The nitrogen functionality trend with temperature and pressure is similar between the hydrogen and hydrogen-oxygen graphene nanoribbon models (Figs. 10 and 12, respectively), demonstrating that the presence of ether groups at the edge of the

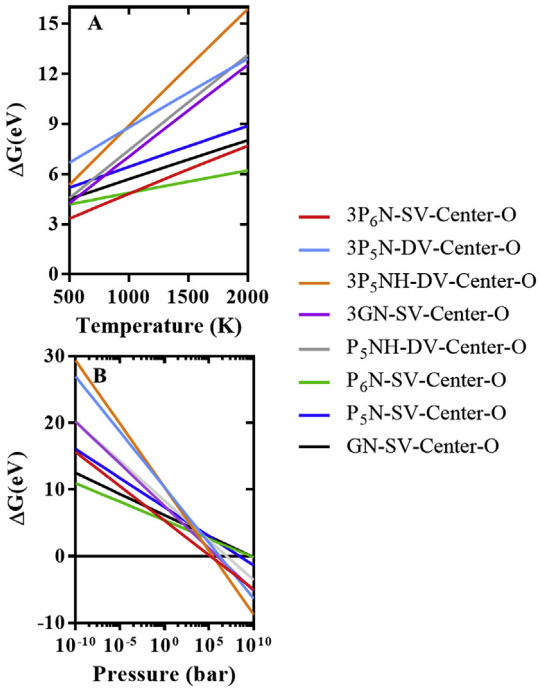

Fig. 12. Phase diagram of nitrogen defect structures on hydrogen-oxygen edge graphene with respect to (A) temperature at 1 bar and (B) pressure at 800 K. The intact hydrogen-oxygen edge graphene model is the reference structure at $\Delta G = 0$ eV in both graphs. Species labels refer to the structures shown in Fig. 11. (A colour version of this figure can be viewed online.)

model does not significantly impact the thermodynamic stability of nitrogen functional groups within the center of the graphene sheet.

The effect of nitrogen functionalization on the electronic structure of the hydrogen-oxygen graphene edge is similar to that noted for the hydrogen graphene edge. As shown in Fig. 4D, the nitrogen defects do not significantly shift the valence band but do induce new states near the Fermi level that are centered on the nitrogen atoms (Fig. 5D). Furthermore, a similar pyridinic concentration effect on the position of the highest occupied nitrogen band

relative to the Fermi level is seen for the hydrogen-oxygen graphene edge (Fig. 5D) as compared to the hydrogen graphene edge (Fig. 5C). A comparison between the $3P_6N$-SV-Center (Fig. 5C) and $3P_6N$-SV-Center-O (Fig. 5D) defects shows that the nitrogen LDOS of a particular defect is not significantly affected by the edge, be it a hydrogen edge or a hydrogen-oxygen edge. This suggests that the simpler graphene models are sufficient for correctly capturing the electronic effects for adsorption on nitrogen functionalized carbon vacancies within the center of graphene.

4. Conclusions

We have examined the thermodynamic stability of nitrogen functional groups on different graphene models using DFT-calculated Gibbs reaction energies. Over a range of conditions and model structures, the most stable nitrogen functionality was pyridinic nitrogen followed by graphitic nitrogen. Pyridinic nitrogen is most easily formed at the graphene edge, but their presence at carbon vacancies in the center of a graphene sheet can have a stabilizing effect on the defective region. At high pressures ($>10^4$ bar), pyrrolic nitrogen structures become the most stable structures. Electronic analyses suggest that the electronic structure of nitrogen functionalities within carbon vacancies in the graphene nanoribbons is unaffected by the presence of a hydrogen or hydrogen-oxygen edge structure. Furthermore, pyridinic nitrogen within vacancy sites create new states near the Fermi level in the graphene, localized on the nitrogen, whose energy can be tuned via the number of incorporated pyridines. The greater thermodynamic stability and availability of electronic states in pyridinic defects make them likely candidates for the binding of metal centers or molecular adsorbates. Overall, this work allows for the identification of temperature and pressure combinations that can be tuned to affect the distribution of nitrogen functional groups in carbonaceous materials during the heat treatment nitrogen doping process with potential applications in the areas of filtrant design, heterogeneous catalysis, and electronics.

Acknowledgements

This work was supported by the National Science Foundation under Contract No. CBET-1703052. This research used resources from the Center for Institutional Research Computing at Washington State University. A portion of the computer time for the computational work was performed using EMSL, a national scientific user facility sponsored by the Department of Energy's Office of Biological and Environmental Research and located at PNNL. PNNL is a multiprogram national laboratory operated for the US DOE by Battelle. The authors thank Greg Collinge, Jacob Bray, and Aidan Garcia for their helpful comments and discussions.

Appendix A. Supplementary data

Supplementary data to this article can be found online at https://doi.org/10.1016/j.carbon.2019.06.019.

References

[1] M. Dresselhaus, G. Dresselhaus, Intercalation compounds of graphite, Adv. Phys. 30 (1981) 139.
[2] G. Duesberg, A. Graham, F. Kreupl, M. Liebau, R. Seidel, E. Unger, W. Hoenlein, Ways towards the scaleable integration of carbon nanotubes into silicon based technology, Diam. Relat. Mater. 13 (2004) 354.
[3] J.C. Tsang, M. Freitag, V. Perebeinos, J. Liu, P. Avouris, Doping and phonon renormalization in carbon nanotubes, Nat. Nanotechnol. 2 (2007) 725.
[4] H.P. Boehm, Chemical Identification of Surface Groups, Adv Catal: Elsevier, 1966, p. 179.
[5] L. Li, P.A. Quinlivan, D.R. Knappe, Effects of activated carbon surface chemistry and pore structure on the adsorption of organic contaminants from aqueous solution, Carbon 40 (2002) 2085.
[6] M. Montes-Morán, D. Suárez, J. Menéndez, E. Fuente, On the nature of basic sites on carbon surfaces: an overview, Carbon 42 (2004) 1219.
[7] T.J. Bandosz, C. Ania, Surface Chemistry of Activated Carbons and its Characterization, Interface Sci Technol: Elsevier, 2006, p. 159.
[8] E. Cruz-Silva, Z. Barnett, B.G. Sumpter, V. Meunier, Structural, magnetic, and transport properties of substitutionally doped graphene nanoribbons from first principles, Phys. Rev. B 83 (2011), 155445.
[9] X. Wang, X. Li, L. Zhang, Y. Yoon, P.K. Weber, H. Wang, J. Guo, H. Dai, N-doping of graphene through electrothermal reactions with ammonia, Science 324 (2009) 768.
[10] C. Zhang, L. Fu, N. Liu, M. Liu, Y. Wang, Z. Liu, Synthesis of nitrogen-doped graphene using embedded carbon and nitrogen sources, Adv. Mater. 23 (2011) 1020.
[11] B. Guo, Q. Liu, E. Chen, H. Zhu, L. Fang, J.R. Gong, Controllable N-doping of graphene, Nano Lett. 10 (2010) 4975.
[12] Y.-C. Lin, C.-Y. Lin, P.-W. Chiu, Controllable graphene N-doping with ammonia plasma, Appl. Phys. Lett. 96 (2010), 133110.
[13] Y. Wang, Y. Shao, D.W. Matson, J. Li, Y. Lin, Nitrogen-doped graphene and its application in electrochemical biosensing, ACS Nano 4 (2010) 1790.
[14] Y. Shao, J. Sui, G. Yin, Y. Gao, Nitrogen-doped carbon nanostructures and their composites as catalytic materials for proton exchange membrane fuel cell, Appl. Catal., B 79 (2008) 89.
[15] R. Lv, M. Terrones, Towards new graphene materials: doped graphene sheets and nanoribbons, Mater. Lett. 78 (2012) 209.
[16] R. Lv, Q. Li, A.R. Botello-Méndez, T. Hayashi, B. Wang, A. Berkdemir, Q. Hao, A.L. Elías, R. Cruz-Silva, H.R. Gutiérrez, Nitrogen-doped graphene: beyond single substitution and enhanced molecular sensing, Sci. Rep. 2 (2012) 586.
[17] A.L.M. Reddy, A. Srivastava, S.R. Gowda, H. Gullapalli, M. Dubey, P.M. Ajayan, Synthesis of nitrogen-doped graphene films for lithium battery application, ACS Nano 4 (2010) 6337.
[18] H. Wang, C. Zhang, Z. Liu, L. Wang, P. Han, H. Xu, K. Zhang, S. Dong, J. Yao, G. Cui, Nitrogen-doped graphene nanosheets with excellent lithium storage properties, J. Mater. Chem. 21 (2011) 5430.
[19] D. Yu, E. Nagelli, F. Du, L. Dai, Metal-free carbon nanomaterials become more active than metal catalysts and last longer, J. Phys. Chem. Lett. 1 (2010) 2165.
[20] J-i Ozaki, Simultaneous doping of boron and nitrogen into a carbon to enhance its oxygen reduction activity in proton exchange membrane fuel cells, Carbon 44 (2006) 3358.
[21] L. Zhang, J. Zhang, D.P. Wilkinson, H. Wang, Progress in preparation of non-noble electrocatalysts for PEM fuel cell reactions, J. Power Sources 156 (2006) 171.
[22] M. Lefèvre, E. Proietti, F. Jaouen, J.-P. Dodelet, Iron-based catalysts with improved oxygen reduction activity in polymer electrolyte fuel cells, Science 324 (2009) 71.
[23] G. Wu, K.L. More, C.M. Johnston, P. Zelenay, High-performance electrocatalysts for oxygen reduction derived from polyaniline, iron, and cobalt, Science 332 (2011) 443.
[24] E. Proietti, F. Jaouen, M. Lefèvre, N. Larouche, J. Tian, J. Herranz, J.-P. Dodelet, Iron-based cathode catalyst with enhanced power density in polymer electrolyte membrane fuel cells, Nat. Commun. 2 (2011) 416.
[25] D.H. Lee, W.J. Lee, W.J. Lee, S.O. Kim, Y.-H. Kim, Theory, synthesis, and oxygen reduction catalysis of Fe-porphyrin-like carbon nanotube, Phys. Rev. Lett. 106 (2011), 175502.
[26] D. Deng, X. Pan, L. Yu, Y. Cui, Y. Jiang, J. Qi, W.-X. Li, Q. Fu, X. Ma, Q. Xue, Toward N-doped graphene via solvothermal synthesis, Chem. Mater. 23 (2011) 1188.
[27] R.I. Jafri, N. Rajalakshmi, S. Ramaprabhu, Nitrogen doped graphene nanoplatelets as catalyst support for oxygen reduction reaction in proton exchange membrane fuel cell, J. Mater. Chem. 20 (2010) 7114.
[28] Y.-H. Lu, M. Zhou, C. Zhang, Y.-P. Feng, Metal-embedded graphene: a possible catalyst with high activity, J. Phys. Chem. C 113 (2009) 20156.
[29] D. Geng, Y. Chen, Y. Chen, Y. Li, R. Li, X. Sun, S. Ye, S. Knights, High oxygen-reduction activity and durability of nitrogen-doped graphene, Energy Environ. Sci. 4 (2011) 760.
[30] H. Xu, D. Cheng, D. Cao, X.C. Zeng, A universal principle for a rational design of single-atom electrocatalysts, Nat. Catal. 10 (2018) 339.
[31] X. Wang, Y. Qin, L. Zhu, H. Tang, Nitrogen-doped reduced graphene oxide as a bifunctional material for removing bisphenols: synergistic effect between adsorption and catalysis, Environ. Sci. Technol. 49 (2015) 6855.
[32] Y. Liu, L. Yu, C.N. Ong, J. Xie, Nitrogen-doped graphene nanosheets as reactive water purification membranes, Nano Res. 9 (2016) 1983.
[33] P. Malik, Dye removal from wastewater using activated carbon developed from sawdust: adsorption equilibrium and kinetics, J. Hazard Mater. 113 (2004) 81.
[34] K. Kadirvelu, M. Kavipriya, C. Karthika, M. Radhika, N. Vennilamani, S. Pattabhi, Utilization of various agricultural wastes for activated carbon preparation and application for the removal of dyes and metal ions from aqueous solutions, Bioresour. Technol. 87 (2003) 129.
[35] X. Wang, N. Zhu, B. Yin, Preparation of sludge-based activated carbon and its application in dye wastewater treatment, J. Hazard Mater. 153 (2008) 22.
[36] S. Babel, T.A. Kurniawan, Cr (VI) removal from synthetic wastewater using coconut shell charcoal and commercial activated carbon modified with oxidizing agents and/or chitosan, Chemosphere 54 (2004) 951.

[37] X. Hu, L. Lei, H.P. Chu, P.L. Yue, Copper/activated carbon as catalyst for organic wastewater treatment, Carbon N. Y. 37 (1999) 631.
[38] A. Ban, A. Schafer, H. Wendt, Fundamentals of electrosorption on activated carbon for wastewater treatment of industrial effluents, J. Appl. Electrochem. 28 (1998) 227.
[39] R.V. Siriwardane, M.-S. Shen, E.P. Fisher, J.A. Poston, Adsorption of CO_2 on molecular sieves and activated carbon, Energy Fuels 15 (2001) 279.
[40] H. Tamon, M. Okazaki, Influence of acidic surface oxides of activated carbon on gas adsorption characteristics, Carbon 34 (1996) 741.
[41] R. Reich, W.T. Ziegler, K.A. Rogers, Adsorption of methane, ethane, and ethylene gases and their binary and ternary mixtures and carbon dioxide on activated carbon at 212-301 K and pressures to 35 atmospheres, Ind. Eng. Chem. 19 (1980) 336.
[42] E. Costa, J. Sotelo, G. Calleja, C. Marron, Adsorption of binary and ternary hydrocarbon gas mixtures on activated carbon: experimental determination and theoretical prediction of the ternary equilibrium data, AlChE J. 27 (1981) 5.
[43] M. Ayiania, F.M. Carbajal-Gamarra, T. Garcia-Perez, C. Frear, W. Suliman, M. Garcia-Perez, Production and characterization of H_2S and PO_4^{3-} carbonaceous adsorbents from anaerobic digested fibers, Biomass Bioenergy 120 (2019) 339.
[44] M. Zhou, Y. Zhai, S. Dong, Electrochemical sensing and biosensing platform based on chemically reduced graphene oxide, Anal. Chem. 81 (2009) 5603.
[45] L. Qu, Y. Liu, J.-B. Baek, L. Dai, Nitrogen-doped graphene as efficient metal-free electrocatalyst for oxygen reduction in fuel cells, ACS Nano 4 (2010) 1321.
[46] J. Wu, D. Zhang, Y. Wang, B. Hou, Electrocatalytic activity of nitrogen-doped graphene synthesized via a one-pot hydrothermal process towards oxygen reduction reaction, J. Power Sources 227 (2013) 185.
[47] B. Zheng, J. Wang, F.-B. Wang, X.-H. Xia, Synthesis of nitrogen doped graphene with high electrocatalytic activity toward oxygen reduction reaction, Electrochem. Commun. 28 (2013) 24.
[48] L. Lai, J.R. Potts, D. Zhan, L. Wang, C.K. Poh, C. Tang, H. Gong, Z. Shen, J. Lin, R.S. Ruoff, Exploration of the active center structure of nitrogen-doped graphene-based catalysts for oxygen reduction reaction, Energy Environ. Sci. 5 (2012) 7936.
[49] G.L. Tian, M.Q. Zhao, D. Yu, X.Y. Kong, J.Q. Huang, Q. Zhang, F. Wei, Nitrogen-doped graphene/carbon nanotube hybrids: in situ formation on bifunctional catalysts and their superior electrocatalytic activity for oxygen evolution/reduction reaction, Small 10 (2014) 2251.
[50] V.B. Parambhath, R. Nagar, S. Ramaprabhu, Effect of nitrogen doping on hydrogen storage capacity of palladium decorated graphene, Langmuir 28 (2012) 7826.
[51] S.A. Giles, Y. Yan, D.G. Vlachos, Effect of substitutionally doped graphene on the activity of metal nanoparticle catalysts for the hydrogen oxidation reaction, ACS Catal. 9 (2019) 1129.
[52] K.C. Kemp, V. Chandra, M. Saleh, K.S. Kim, Reversible CO_2 adsorption by an activated nitrogen doped graphene/polyaniline material, Nanotechnology 24 (2013), 235703.
[53] M. Saleh, V. Chandra, K.C. Kemp, K.S. Kim, Synthesis of N-doped microporous carbon via chemical activation of polyindole-modified graphene oxide sheets for selective carbon dioxide adsorption, Nanotechnology 24 (2013), 255702.
[54] H.M. Lee, I.S. Youn, M. Saleh, J.W. Lee, K.S. Kim, Interactions of CO_2 with various functional molecules, Phys. Chem. Chem. Phys. 17 (2015) 10925.
[55] S. Lee, M. Lee, Y.-C. Chung, Geometric and magnetic properties of Co adatom decorated nitrogen-doped graphene, J. Appl. Phys. 113 (2013), 17B503.
[56] A.S. Rad, A. Shadravan, A.A. Soleymani, N. Motaghedi, Lewis acid-base surface interaction of some boron compounds with N-doped graphene; first principles study, Curr. Appl. Phys. 15 (2015) 1271.
[57] H-p Zhang, X-g Luo, X-y Lin, X. Lu, Y. Leng, H-t Song, Density functional theory calculations on the adsorption of formaldehyde and other harmful gases on pure, Ti-doped, or N-doped graphene sheets, Appl. Surf. Sci. 283 (2013) 559.
[58] P. Lambin, H. Amara, F. Ducastelle, L. Henrard, Long-range interactions between substitutional nitrogen dopants in graphene: electronic properties calculations, Phys. Rev. B 86 (2012), 045448.
[59] L. Yu, X. Pan, X. Cao, P. Hu, X. Bao, Oxygen reduction reaction mechanism on nitrogen-doped graphene: a density functional theory study, J. Catal. 282 (2011) 183.
[60] M.D. Bhatt, G. Lee, J.S. Lee, Density functional theory (DFT) calculations for oxygen reduction reaction mechanisms on metal-, nitrogen-co-doped graphene (M-N_2-G (M= Ti, Cu, Mo, Nb and Ru)) electrocatalysts, Electrochim. Acta 228 (2017) 619.
[61] M. Li, L. Zhang, Q. Xu, J. Niu, Z. Xia, N-doped graphene as catalysts for oxygen reduction and oxygen evolution reactions: theoretical considerations, J. Catal. 314 (2014) 66.
[62] B. Lu, T.J. Smart, D. Qin, J.E. Lu, N. Wang, L. Chen, Y. Peng, Y. Ping, S. Chen, Nitrogen and iron-codoped carbon hollow nanotubules as high-performance catalysts toward oxygen reduction reaction: a combined experimental and theoretical study, Chem. Mater. 29 (2017) 5617.
[63] H. Kim, K. Lee, S.I. Woo, Y. Jung, On the mechanism of enhanced oxygen reduction reaction in nitrogen-doped graphene nanoribbons, Phys. Chem. Chem. Phys. 13 (2011) 17505.
[64] H. Yan, B. Xu, S. Shi, C. Ouyang, First-principles study of the oxygen adsorption and dissociation on graphene and nitrogen doped graphene for Li-air batteries, J. Appl. Phys. 112 (2012), 104316.
[65] C. Ma, X. Shao, D. Cao, Nitrogen-doped graphene nanosheets as anode materials for lithium ion batteries: a first-principles study, J. Mater. Chem. 22 (2012) 8911.
[66] Y. Zheng, Y. Jiao, L. Ge, M. Jaroniec, S.Z. Qiao, Two-step boron and nitrogen doping in graphene for enhanced synergistic catalysis, Angew. Chem. Int. Ed. 125 (2013) 3192.
[67] J. Liang, Y. Jiao, M. Jaroniec, S.Z. Qiao, Sulfur and nitrogen dual-doped mesoporous graphene electrocatalyst for oxygen reduction with synergistically enhanced performance, Angew. Chem. Int. Ed. 124 (2012) 11664.
[68] L. Zhang, Z. Xia, Mechanisms of oxygen reduction reaction on nitrogen-doped graphene for fuel cells, J. Phys. Chem. C 115 (2011) 11170.
[69] L.-C. Yin, J. Liang, G.-M. Zhou, F. Li, R. Saito, H.-M. Cheng, Understanding the interactions between lithium polysulfides and N-doped graphene using density functional theory calculations, Nanomater. Energy 25 (2016) 203.
[70] M. Yang, L. Wang, M. Li, T. Hou, Y. Li, Structural stability and O_2 dissociation on nitrogen-doped graphene with transition metal atoms embedded: a first-principles study, AIP Adv. 5 (2015), 067136.
[71] A. Zitolo, V. Goellner, V. Armel, M.-T. Sougrati, T. Mineva, L. Stievano, E. Fonda, F. Jaouen, Identification of catalytic sites for oxygen reduction in iron-and nitrogen-doped graphene materials, Nat. Mater. 14 (2015) 937.
[72] S. Kabir, K. Artyushkova, A. Serov, B. Kiefer, P. Atanassov, Binding energy shifts for nitrogen-containing graphene-based electrocatalysts—experiments and DFT calculations, Surf. Interface Anal. 48 (2016) 293.
[73] Y. Fujimoto, S. Saito, Formation, stabilities, and electronic properties of nitrogen defects in graphene, Phys. Rev. B 84 (2011), 245446.
[74] C.L. Mangun, K.R. Benak, J. Economy, K.L. Foster, Surface chemistry, pore sizes and adsorption properties of activated carbon fibers and precursors treated with ammonia, Carbon 39 (2001) 1809.
[75] W. Chen, F.S. Cannon, J.R. Rangel-Mendez, Ammonia-tailoring of GAC to enhance perchlorate removal. II: perchlorate adsorption, Carbon 43 (2005) 581.
[76] G. Kresse, J. Hafner, Ab initio molecular dynamics for liquid metals, Phys. Rev. B 47 (1993) 558.
[77] G. Kresse, J. Furthmüller, Efficiency of ab-initio total energy calculations for metals and semiconductors using a plane-wave basis set, Comput. Mater. Sci. 6 (1996) 15.
[78] G. Kresse, J. Furthmüller, Efficient iterative schemes for ab initio total-energy calculations using a plane-wave basis set, Phys. Rev. B 54 (1996) 11169.
[79] G. Kresse, D. Joubert, From ultrasoft pseudopotentials to the projector augmented-wave method, Phys. Rev. B 59 (1999) 1758.
[80] A.J. Hensley, J. Zhang, I. Vinçon, X.P. Hernandez, D. Tranca, G. Seifert, J.-S. McEwen, Y. Wang, Mechanistic understanding of methanol carbonylation: interfacing homogeneous and heterogeneous catalysis via carbon supported Ir La, J. Catal. 361 (2018) 414.
[81] J.P. Perdew, K. Burke, M. Ernzerhof, Generalized gradient approximation made simple, Phys. Rev. Lett. 77 (1996) 3865.
[82] C. Isvoranu, J. Åhlund, B. Wang, E. Ataman, N. Mårtensson, C. Puglia, J.N. Andersen, M.-L. Bocquet, J. Schnadt, Electron spectroscopy study of the initial stages of iron phthalocyanine growth on highly oriented pyrolitic graphite, J. Chem. Phys. 131 (2009), 214709.
[83] I.C. Gerber, A.V. Krasheninnikov, A.S. Foster, R.M. Nieminen, A first-principles study on magnetic coupling between carbon adatoms on graphene, New J. Phys. 12 (2010), 113021.
[84] F. Mehmood, R. Pachter, W. Lu, J.J. Boeckl, Adsorption and diffusion of oxygen on single-layer graphene with topological defects, J. Phys. Chem. 117 (2013) 10366.
[85] A. Pulido, M. Boronat, A. Corma, Theoretical investigation of gold clusters supported on graphene sheets, New J. Chem. 35 (2011) 2153.
[86] Z. Hou, X. Wang, T. Ikeda, K. Terakura, M. Oshima, M-a Kakimoto, S. Miyata, Interplay between nitrogen dopants and native point defects in graphene, Phys. Rev. B 85 (2012) 165439.
[87] H.J. Monkhorst, J.D. Pack, Special points for Brillouin-zone integrations, Phys. Rev. B 13 (1976) 5188.
[88] K. Momma, F. Izumi, VESTA 3 for three-dimensional visualization of crystal, volumetric and morphology data, J. Appl. Crystallogr. 44 (2011) 1272.
[89] M.W. Smith, I. Dallmeyer, T.J. Johnson, C.S. Brauer, J.-S. McEwen, J.F. Espinal, M. Garcia-Perez, Structural analysis of char by Raman spectroscopy: improving band assignments through computational calculations from first principles, Carbon 100 (2016) 678.
[90] M. Smith, L. Scudiero, J. Espinal, J.-S. McEwen, M. Garcia-Perez, Improving the deconvolution and interpretation of XPS spectra from chars by ab initio calculations, Carbon 110 (2016) 155.
[91] D. Ugarte, Curling and closure of graphitic networks under electron-beam irradiation, Nature 359 (1992) 707.
[92] M. Terrones, H. Terrones, F. Banhart, J.-C. Charlier, P. Ajayan, Coalescence of single-walled carbon nanotubes, Science 288 (2000) 1226.
[93] J.A. Rodriguez-Manzo, F. Banhart, Creation of individual vacancies in carbon nanotubes by using an electron beam of 1 Å diameter, Nano Lett. 9 (2009) 2285.
[94] A. Krasheninnikov, F. Banhart, Engineering of nanostructured carbon materials with electron or ion beams, Nat. Mater. 6 (2007) 723.
[95] M.H. Gass, U. Bangert, A.L. Bleloch, P. Wang, R.R. Nair, A. Geim, Free-standing graphene at atomic resolution, Nat. Nanotechnol. 3 (2008) 676.
[96] A. Hashimoto, K. Suenaga, A. Gloter, K. Urita, S. Iijima, Direct evidence for

atomic defects in graphene layers, Nature 430 (2004) 870.
[97] P.A. Denis, Organic chemistry of graphene: the Diels–Alder reaction, Chem. Eur J. 19 (2013) 15719.
[98] G.-D. Lee, C. Wang, E. Yoon, N.-M. Hwang, D.-Y. Kim, K. Ho, Diffusion, coalescence, and reconstruction of vacancy defects in graphene layers, Phys. Rev. Lett. 95 (2005), 205501.
[99] J.C. Meyer, C. Kisielowski, R. Erni, M.D. Rossell, M. Crommie, A. Zettl, Direct imaging of lattice atoms and topological defects in graphene membranes, Nano Lett. 8 (2008) 3582.
[100] J.H. Warner, M.H. Rümmeli, T. Gemming, B. Büchner, G.A.D. Briggs, Direct imaging of rotational stacking faults in few layer graphene, Nano Lett. 9 (2008) 102.
[101] A. Chuvilin, J.C. Meyer, G. Algara-Siller, U. Kaiser, From graphene constrictions to single carbon chains, New J. Phys. 11 (2009), 083019.
[102] M.W. Smith, G. Helms, J.-S. McEwen, M. Garcia-Perez, Effect of pyrolysis temperature on aromatic cluster size of cellulose char by quantitative multi cross-polarization 13 C NMR with long range dipolar dephasing, Carbon N. Y. 116 (2017) 210.
[103] M. Chase, J.L. Curnutt, A. Hu, H. Prophet, A. Syverud, L. Walker, JANAF thermochemical tables, 1974 supplement, J. Phys. Chem. Ref. Data 3 (1974) 311.
[104] A. Bajpai, P. Mehta, K. Frey, A.M. Lehmer, W.F. Schneider, Benchmark first-principles calculations of adsorbate free energies, ACS Catal. 8 (2018) 1945.
[105] Groden K, Collinge G, McEwen J-S. (Unpublished results). 2019.
[106] X.-F. Li, K.-Y. Lian, L. Liu, Y. Wu, Q. Qiu, J. Jiang, M. Deng, Y. Luo, Unraveling the formation mechanism of graphitic nitrogen-doping in thermally treated graphene with ammonia, Sci. Rep. 6 (2016) 23495.
[107] R. Czerw, M. Terrones, J.-C. Charlier, X. Blase, B. Foley, R. Kamalakaran, N. Grobert, H. Terrones, D. Tekleab, P. Ajayan, Identification of electron donor states in N-doped carbon nanotubes, Nano Lett. 1 (2001) 457.
[108] Y. Zhang, J. Ge, L. Wang, D. Wang, F. Ding, X. Tao, W. Chen, Manageable N-doped graphene for high performance oxygen reduction reaction, Sci. Rep. 3 (2013) 2771.
[109] M. Smith, S. Ha, J.E. Amonette, I. Dallmeyer, M. Garcia-Perez, Enhancing cation exchange capacity of chars through ozonation, Biomass Bioenergy 81 (2015) 304.
[110] W. Suliman, J.B. Harsh, N.I. Abu-Lail, A.-M. Fortuna, I. Dallmeyer, M. Garcia-Perez, Modification of biochar surface by air oxidation: role of pyrolysis temperature, Biomass Bioenergy 85 (2016) 1.